

ALMA DETECTED OVERDENSITY OF SUB-MILLIMETER SOURCES AROUND WISE/NVSS-SELECTED $z \sim 2$ DUSTY QUASARS

ANDREA SILVA^{1,2}, ANNA SAJINA¹, CAROL LONSDALE³, AND MARK LACY³

¹Department of Physics and Astronomy, Tufts University, Medford, MA 02155, USA

²National Astronomical Observatory of Japan 2-21-1 Osawa, Mitaka, Tokyo 181-8588, Japan

³National Radio Astronomy Observatory, 520 Edgemont Road, Charlottesville, VA 22903, USA

Received 2015 March 24; accepted 2015 May 16; published 2015 June 15

ABSTRACT

We study the environments of 49 *WISE*/*NVSS*-selected dusty, hyper-luminous, $z \sim 2$ quasars using the Atacama Large Millimeter/Sub-millimeter Array (ALMA) 345 GHz images. We find that 17 of the 49 *WISE*/*NVSS* sources show additional sub-millimeter galaxies within the ALMA primary beam, probing scales within ~ 150 kpc. We find a total of 23 additional sub-millimeter sources, four of which are in the field of a single *WISE*/*NVSS* source. The measured 870 μm source counts are $\sim 10\times$ what is expected for unbiased regions, suggesting such hyper-luminous dusty quasars are excellent at probing high-density peaks.

Key words: galaxies: active – galaxies: clusters: general – galaxies: evolution

1. INTRODUCTION

Clusters are the largest gravitationally bound objects in the universe. Finding clusters, especially at higher redshifts, is therefore critical both for constraining models of structure formation (e.g., Poggianti et al. 2010) and for studying the role of environment in galaxy evolution (e.g., Peng et al. 2012). However, finding high- z clusters is challenging. For example, optical-color-based techniques (Gladders & Yee 2005) rely on the red-sequence galaxies that dominate the core cluster populations, but only up to $z \sim 1.5$ (Lidman et al. 2008; Mei et al. 2009). At $z \sim 2$, the universe is only ~ 3.3 Gyr old, i.e., insufficient time for a galaxy with a velocity of few hundred km s^{-1} to have crossed cluster-scale structures (a few megaparsecs). Hence, any overdense structure detected would likely be protoclusters still in the process of virialization, hindering X-ray and Sunyaev–Zeldovich detection techniques. Spectroscopic and photometric redshift surveys that are deep enough to reach cosmologically interesting distances do not yet sample sufficient volumes to reach the largest possible clusters in a systematic way (Geach et al. 2011; Yuan et al. 2014). We can avoid these issues by using strongly biased populations such as QSOs (Priddey et al. 2008; Stevens et al. 2010; Falder et al. 2011), although see Fanidakis et al. (2013) for an alternative view, and radio galaxies (Wylezalek et al. 2013; Dannerbauer et al. 2014) to find high- z overdensities of star-forming galaxies. For example, an excess of sub-millimeter galaxies (SMGs; see Blain et al. 2002 for a review) is observed in the fields of high-redshift radio galaxies (HzRGs; Ivison et al. 2000; Stevens et al. 2003; Dannerbauer et al. 2014). Since SMGs are believed to be the progenitors of local elliptical galaxies (Smail et al. 2004; Ivison et al. 2013), this excess is consistent with the view that we are observing protoclusters at the time of build-up of their elliptical galaxy populations, with the central radio galaxy likely to evolve into the brightest cluster galaxy (BCG; Miley et al. 2006). The higher angular resolution of Atacama Large Millimeter/Sub-millimeter Array (ALMA) opens the door for the first time to look for SMG overdensities in the near vicinity ($\lesssim 100$ kpc) of potential proto-cluster markers. This higher resolution has also shed light into the bright end of the SMG population. For instance, Karim et al. (2013) found a significant deficit of source counts above

~ 8 mJy compared with single-dish surveys and concluded that even at $S_{850\mu\text{m}} \gtrsim 4$ mJy, SMGs often reveal multiple distinct sources in higher-resolution images.

In this Letter, we compute the sub-millimeter galaxy source counts in the near vicinity of 49 *WISE*/*NVSS*-selected $z \sim 2$, dusty, hyper-luminous ($L_{\text{IR}} \gtrsim 10^{13} L_{\odot}$), moderately radio-loud quasars (Lonsdale et al. 2015, hereinafter L15) in order to study their environments as well as the potential effect of those rare, highly obscured quasars on their surroundings.

Throughout this Letter, we adopt *Planck* cosmology values (Planck Collaboration et al. 2014) of $H_0 = 67.3 \text{ km s}^{-1} \text{ Mpc}^{-1}$, $\Omega_m = 0.315$, and $\Omega_{\Lambda} = 0.685$.

2. SAMPLE SELECTION

Full details on the sample selection are given in L15. The parent sample of 165 sources was selected on the basis of *WISE* 22 μm and *NVSS* 1.4 GHz detection, extremely red *WISE* [3.4]–[4.6] and [4.6]–[12] colors, and $\log(f_{20\text{cm}}/f_{22\mu\text{m}}) > 0$ (i.e., systems where the active galactic nucleus (AGN) dominates the radio emission). Their *WISE* colors imply obscured AGNs typically at $z \gtrsim 1$ (see also Jarrett et al. 2011; Yan et al. 2013). The 22 μm detection implies rare, hyper-luminous ($L_{\text{IR}} > 10^{13} L_{\odot}$) galaxies. The sample further focuses on higher- z sources by excluding optically bright and extended sources.

The ALMA-observed sub-sample of 49 was selected before the rest of the *WISE*/*NVSS* sample and differs slightly from the full sample (L15). In particular, it is limited to $\log(f_{20\text{cm}}/f_{22\mu\text{m}}) < 1$ sources, avoiding radio-loud systems; its [3.4]–[4.6] colors are marginally redder, implying dustier AGNs; and it reaches 22 μm flux densities that are 0.2 dex fainter than the full sample. We examined the effect of the latter by looking at our results if the fainter sources in the ALMA sub-sample are excluded and found no significant difference. Therefore, our results translate to the full *WISE*/*NVSS* sample, modulo the minority therein that are radio loud (13%) and/or have slightly bluer [3.6]–[4.5] colors (9%). Optical spectroscopic redshifts are available for 43 of the 49 ALMA sources and range from ~ 0.47 to 2.85, with a mean redshift of $\langle z \rangle = 1.69$.

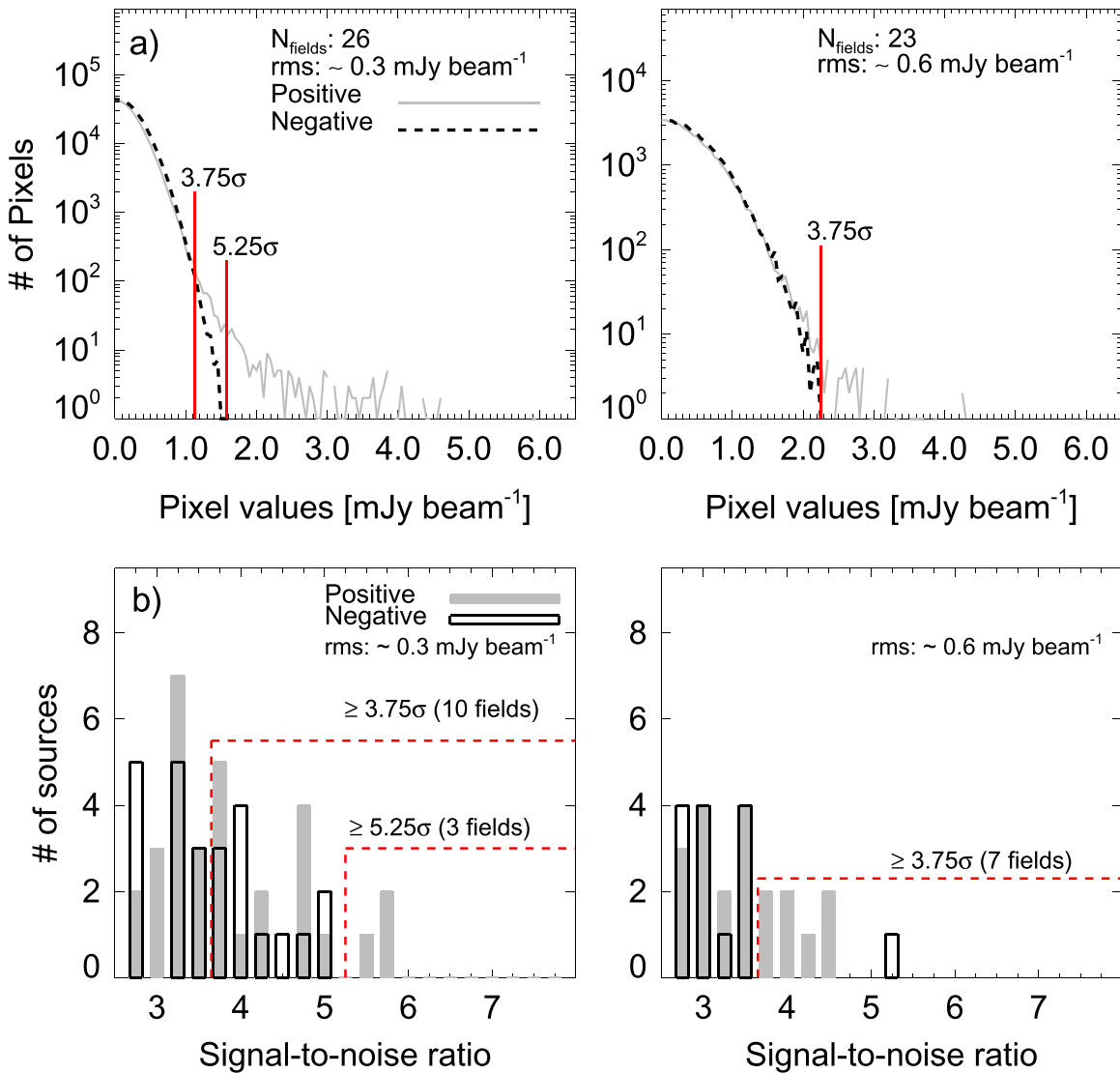


Figure 1. Top: pixel histograms for fields with different rms values before primary beam correction. Bottom: histogram of the signal-to-noise ratio (S/N) of sources extracted in the “positive” and “negative” images in the 49 *WISE*/NVSS fields. The threshold of $S/N = 3.75$, adopted when “positive” sources exceeded the number of “negative” sources, is indicated by the red lines. We also show the high-confidence cut (Section 4.1). In parentheses, we indicate the number of fields in which the sources with that threshold were detected.

3. OBSERVATIONS AND DATA REDUCTION

The ALMA observations were conducted in three epochs: 23 sources on 2011 November 16, 14 on 2012 May 25, and 12 on 2012 August 28. In each case, the observations were conducted in Band 7 (345 GHz) with an 8 GHz bandwidth. The time on source was ~ 1.5 minutes per object. The different number of antennae available (15, 19, and 23, respectively) led to different beam sizes and rms values. Specifically, the synthesized beam sizes are $1''.24$, $0''.55$, and $0''.45$ for each run. By placing multiple apertures at random position in the images, we obtain the average rms values for each run, which are 0.60, 0.30, and 0.32 mJy beam^{-1} , respectively, and they do not significantly vary within the primary beam uncorrected for attenuation.⁴ The primary beam size for ALMA at 345 GHz is $18''.2$. At the mean redshift of this sample, $\langle z \rangle = 1.69$, this

⁴ The target rms was $0.5 \text{ mJy beam}^{-1}$; however, as new antennae were added, the observations reached deeper rms.

primary beam size corresponds to ~ 158 kpc. The data were reduced using standard procedures and the Common Astronomy Software, *CASA* (McMullin et al. 2007). Twenty-six of the 49 *WISE*/NVSS sources were detected above a 3σ level, and none of them is resolved. For further details on the observations and data reduction, see L15.

4. RESULTS

4.1. Identifying Field Sources

Figure 1 (top) shows the pixel histograms, before primary beam correction, grouped by rms value. We include all pixels within the primary beam and outside a $1''.5$ radius of the center of the images to avoid the emission from the targeted *WISE*/NVSS sources. The histograms show an excess of positive pixels starting at 3.75σ . Although, a full P(D) analysis (e.g., Patanchon et al. 2009; Glenn et al. 2010) is beyond the scope of this paper, this excess confirms the presence of field sources.

Table 1
Basic Properties of the SMGs Identified in the Fields of the 49 *WISE/NVSS*-selected Targets

| <i>WISE/NVSS</i> Field Name ^a | ID in Figure 2 | R.A. (J2000) (h:m:s) | Decl. (J2000) (d:m:s) | $S_{870\ \mu\text{m}}^b$ (mJy) | S/N | D^c (") | z^d | D^e (kpc) | A_T (arcmin ²) | Detect. ^f |
|---|-------------------|-------------------------|--------------------------|-----------------------------------|------|--------------|-------|----------------|---------------------------------|----------------------|
| (J035448.24–330827) | 1 | 03:54:48.62 | –33:08:27.70 | 2.29 ± 0.58 | 3.98 | 5.1 | 1.373 | 44 | 0.25 | No |
| (J051905.84–081320) | 2 | 05:19:05.62 | –08:13:28.62 | 4.53 ± 1.13 | 4.31 | 8.8 | 2.000 | 76 | 1.62 | No |
| (J053622.59–270300) | 3 | 05:36:22.24 | –27:03:00.73 | 2.47 ± 0.69 | 3.76 | 4.7 | 1.791 | 41 | 0.37 | Yes |
| (J061405.55–093658) | 4 | 06:14:05.37 | –09:37:06.57 | 4.23 ± 1.07 | 4.05 | 8.3 | 2.000 | 71 | 1.56 | No |
| (J063027.81–212058) | 5 | 06:30:27.72 | –21:20:51.39 | 4.81 ± 1.08 | 4.60 | 7.2 | 1.439 | 42 | 1.65 | Yes |
| (J064228.93–272801) | 6 | 06:42:29.00 | –27:27:56.61 | 3.15 ± 0.84 | 3.80 | 5.1 | 1.340 | 44 | 0.97 | Yes |
| (J070257.20–280842) | 7 | 07:02:56.89 | –28:08:42.30 | 3.22 ± 0.70 | 4.73 | 3.7 | 0.943 | 30 | 1.01 | No |
| J130817.00–344754 | 8 | 13:08:17.52 | –34:47:53.14 | $1.83 \pm 0.54(2.12)$ | 3.86 | 6.3 | 1.652 | 55 | 1.25 | Yes |
| (J143419.59–023543) | 9 | 14:34:19.30 | –02:35:36.48 | 2.92 ± 0.63 | 5.77 | 8.4 | 1.922 | 72 | 1.86 | Yes |
| J143931.76–372523 | 10 | 14:39:32.42 | –37:25:23.25 | $1.71 \pm 0.49(1.98)$ | 3.85 | 7.9 | 1.200 | 67 | 1.06 | No |
| J143931.76–372523 | 11 | 14:39:31.60 | –37:25:30.91 | $2.06 \pm 0.60(2.27)$ | 4.80 | 7.7 | 1.200 | 66 | 1.55 | No |
| J151003.71–220311 | 12 | 15:10:03.76 | –22:03:04.51 | $1.30 \pm 0.38(1.59)$ | 3.75 | 5.2 | 0.950 | 42 | 0.37 | No |
| J151003.71–220311 | 13 | 15:10:04.14 | –22:03:11.90 | $1.87 \pm 0.45(2.11)$ | 4.91 | 6.2 | 0.950 | 50 | 1.29 | No |
| J151003.71–220311 | 14 | 15:10:04.28 | –22:03:13.51 | $2.33 \pm 0.65(2.70)$ | 4.44 | 8.7 | 0.950 | 71 | 1.74 | No |
| J151003.71–220311 | 15 | 15:10:03.50 | –22:03:15.26 | $1.68 \pm 0.39(1.92)$ | 4.40 | 6.2 | 0.950 | 51 | 0.99 | No |
| J151424.12–341100 | 16 | 15:14:23.84 | –34:10:55.03 | $1.78 \pm 0.49(1.99)$ | 4.81 | 6.0 | 1.080 | 50 | 1.15 | No |
| (J152116.59+001755) | 17 | 15:21:16.03 | +00:17:54.20 | 3.04 ± 0.82 | 5.86 | 8.3 | 0.700 | 61 | 1.87 | Yes |
| J154141.64–114409 | 18 | 15:41:42.17 | –11:44:07.85 | $1.82 \pm 0.61(2.22)$ | 3.76 | 7.8 | 1.580 | 68 | 1.22 | Yes |
| (J163426.87–172139) | 19 | 16:34:26.67 | –17:21:36.05 | $1.90 \pm 0.44(2.03)$ | 5.57 | 4.8 | 2.070 | 41 | 1.36 | No |
| J163426.87–172139 | 20 | 16:34:27.34 | –17:21:41.47 | $2.15 \pm 0.47(2.36)$ | 5.07 | 7.0 | 2.070 | 60 | 1.62 | No |
| J164107.22–054827 | 21 | 16:41:06.80 | –05:48:30.97 | $1.78 \pm 0.53(2.14)$ | 3.91 | 7.4 | 1.830 | 64 | 1.15 | Yes |
| J170204.65–081108 | 22 | 17:02:04.51 | –08:11:08.51 | $1.65 \pm 0.44(1.80)$ | 4.80 | 2.2 | 2.850 | 18 | 0.97 | No |
| J170204.65–081108 | 23 | 17:02:04.65 | –08:11:13.95 | $1.88 \pm 0.60(2.09)$ | 4.13 | 6.1 | 2.850 | 49 | 1.35 | No |

Notes. The fields are separated by high (top) and low rms values (bottom).

^a In parentheses, the sources selected with the high-confidence level (Section 4.1).

^b De-boosted and primary beam corrected flux density. Errors are obtained by adding in quadrature of the errors obtained in IMFIT and the rms values at the position of the serendipitous source after primary beam correction. The boosted fluxes are shown in parentheses.

^c Angular distance of the source from the target *WISE/NVSS* source’s position.

^d Redshift *WISE/NVSS* target.

^e Physical separation between the new detected SMG and the *WISE/NVSS* target, assuming they are at the same redshift.

^f Detection *WISE/NVSS* target above the 3σ level.

We generate negatives of all the images and use SExtractor (Bertin & Arnouts 1996) to find all $>2\sigma$ “sources” in both our positive and negative maps. We only select sources within the primary beam. Before primary beam correction, we measure flux densities and associated uncertainties of all SExtractor-selected sources using IMFIT in CASA. Figure 1 (bottom) shows histograms in signal to noise of these “positive” and “negative” sources. Beyond 3.75σ , the “positive” sources are in excess for both rms groups. Using this threshold, we detect 23 sources in 17 fields.⁵ We refer to this as our “primary” serendipitous source sample. However, the spurious source fraction (as implied by the presence of “negative” sources above this signal-to-noise ratio (S/N) threshold) is non-negligible. None of the images shows obvious issues that may account for these such as insufficient cleaning. We compute the spurious fraction as $N_{\text{neg}}/(N_{\text{pos}} + N_{\text{neg}})$, where N_{neg} is the number of “negative” sources above 3.75σ and N_{pos} is the number of “positive” sources above this threshold. The result is a spurious fraction of 42% and 12% for images with an rms of 0.3 and 0.6 mJy beam^{−1}, respectively. Because of the high spurious fraction among the lower-rms fields, we also consider a more conservative cut where we only keep sources with an

$S/N > 5.25\sigma$ in these lower-rms fields.⁶ This leaves us with a total of 10 sources spread among 10 fields. We refer to this as our “high-confidence” serendipitous source sample. In either case, this spurious source fraction is taken into account in computing the source counts (Section 4.3).

Figure 2 shows the fields with the 23 positive sources that we identify in the primary serendipitous source sample (i.e., with an $S/N > 3.75\sigma$). The properties of the central *WISE/NVSS* sources themselves are addressed in L15 (note 13 fields have no detections at all). The detected sources are unresolved, and none of them has been previously identified, based on a search on NED.⁷ Their fluxes, uncorrected for primary beam attenuation, range from 1.56 to 3.11 mJy.⁸ The key parameters for all the sources are presented in Table 1. Based on blank-field counts, we expect $\sim 0.04(0.02)$ sources/field in the rms $\sim 0.3(0.6)$ mJy fields, respectively. Without any further analysis, our observations show that 30% of fields already have

⁶ A change in pixel size from $0''.1$ to $0''.25$ in the lower-rms fields (thus matching the higher-rms fields) does not affect our results.

⁷ Nasa Extragalactic Database; <http://ned.ipac.caltech.edu/>

⁸ We apply a primary beam correction using $F_{\text{pbc}} = F_0 \exp\left(4 \ln(2) \frac{d^2}{\theta^2}\right)$, where F_{pbc} is the corrected flux, F_0 is the uncorrected flux, θ is the primary beam size, and d is the distance of the source from the center of the image.

⁵ Eight of these 17 *WISE/NVSS* sources present emission above the 3σ level; see Table 1.

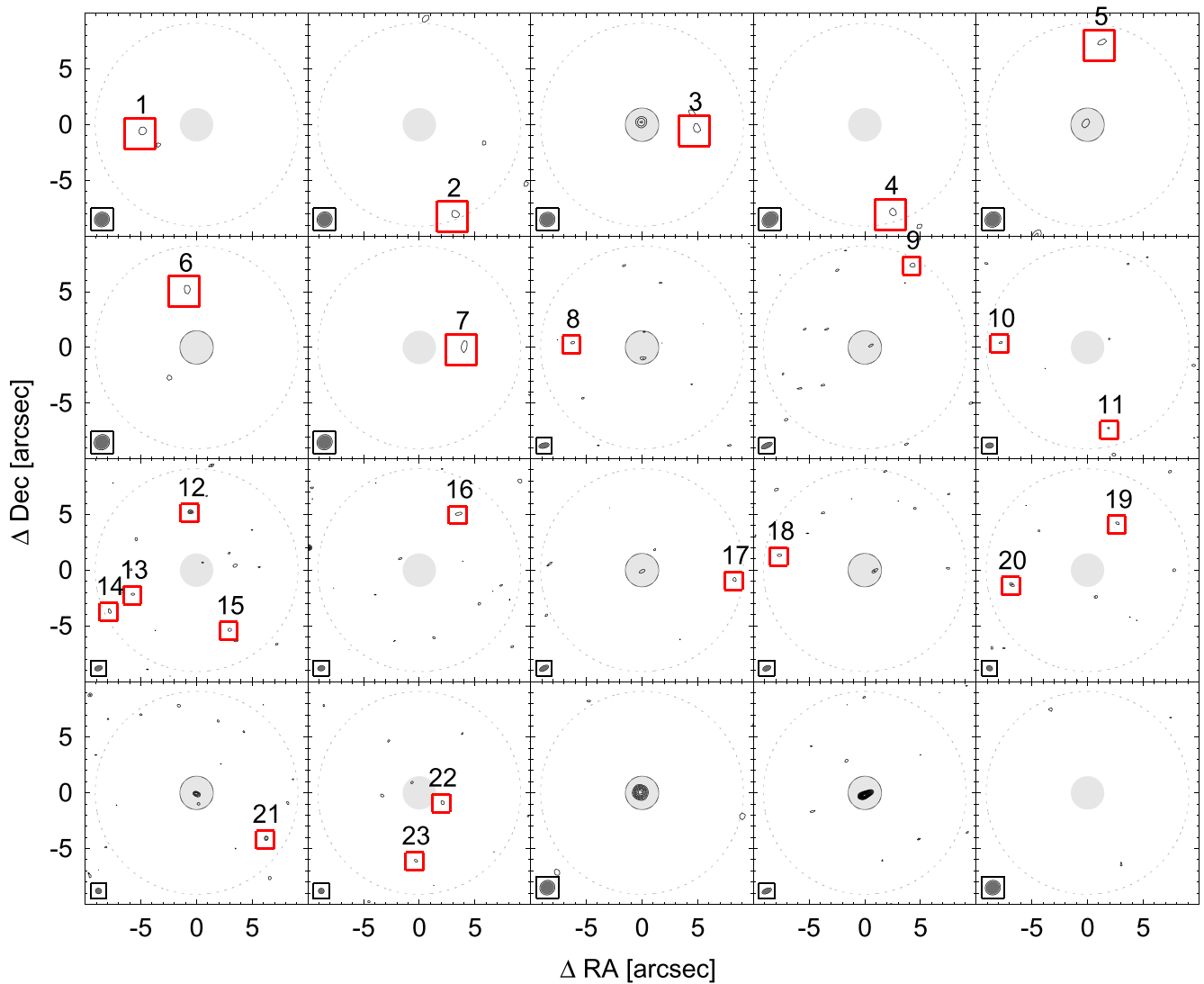


Figure 2. $870\ \mu\text{m}$ continuum maps in which field sub-millimeter sources are identified around the *WISE/NVSS*-selected targets. We include three fields with no additional source detection (bottom right in the image). Contours start at the 3σ level and are in steps of 1σ . The identified sources with $S/N > 3.75$ (Section 4.1) are boxed and labeled with an ID number (Table 1). The gray circles at the center of the images indicate the area where we do not search for sources, i.e., the location of the *WISE/NVSS* targets, and those with $S/N > 3$ are indicated with the circle around the gray region. The synthesized beam is shown at the bottom left of the images. The primary beam size is indicated by the dashed circles.

at least one serendipitous source, which implies counts are $\sim 10\times$ in excess of blank-sky sub-millimeter counts. The existence of fields without serendipitous detections is consistent with our estimated counts that imply a probability of finding a source to be < 1 in any given field.

4.2. Angular Distribution of Serendipitous Sources

For each field, we calculate the cumulative number of detected sources at different angular radii. We plot the mean of these cumulative fractions and compare with the expected fraction of sources with no angular clustering (Figure 3). For the primary serendipitous sample, we find no evidence of angular clustering, which would manifest as an excess of sources toward the central source, relative to a random distribution. This is consistent with the result of Jones et al. (2015), toward a sub-sample of our same parent population of 30 red *WISE/NVSS* sources observed with SCUBA at $850\ \mu\text{m}$. They sample angular scales that start at our external radius and extend up to $1.5\ \text{arcmin}$. Our high-confidence sample even

shows a tentative sign of a dearth of SMGs in the vicinity of the *WISE/NVSS* sources. This may be the result of feedback effects from the central source quenching star formation in the near vicinity. However, given our error bars, the significance of this result is only $\sim 2\sigma$ and needs further investigation before it is conclusive.

4.3. Source Counts

We calculate the integral source counts $N(>S)$ for the additional sub-millimeter sources by following the method described in Ono et al. (2014):

$$N(>S) = \sum_{S_i > S} \frac{1 - f_c(S_i)}{C(S_i)A_T(S_i)}. \quad (1)$$

The fraction of spurious sources $f_c(S_i)$ is 12% and 42% for our primary serendipitous source sample, which we treat as a constant for fields with the same rms values. The completeness $C(S_i)$ is calculated by injecting 50 artificial sources at random

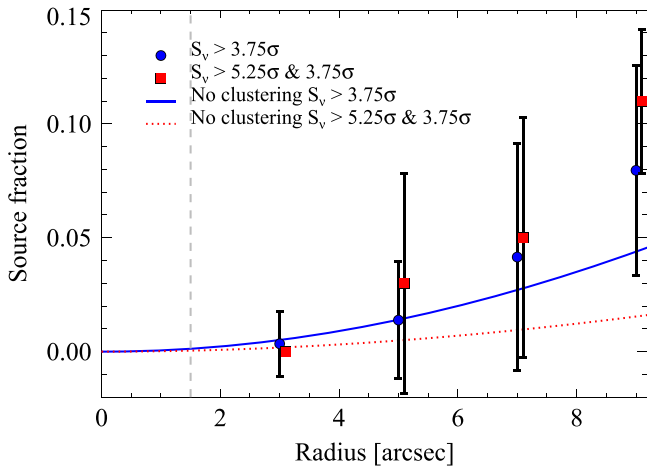


Figure 3. Circles and squares (shifted to the right by $0''.1$) represent the cumulative fraction of detected sources in each field within different radii obtained for the different selection thresholds (as indicated). The solid and dotted lines indicate the expected number of serendipitous sources if they are randomly located with no angular clustering. The interior limit of source detection is $1''.5$.

positions in an image where all sources with an $S/N \geq 3.0$ are removed. This is performed for two images representing the two different rms values. The procedure is repeated 1000 times, and then completeness is computed from the fraction of recovered sources at different flux densities. Above 3σ , completeness ranges from 85% to 100% and is applied before primary beam correction. The effective area is the area in which a source with intrinsic flux density S_i will be detected in one field. The total effective area $A_T(S_i)$ is the addition of the effective areas in all the fields with similar rms values, i.e., for a given flux density, we add the effective areas of all fields with either rms of 0.3 or 0.6 mJy beam $^{-1}$. Their values are presented in Table 1. We estimate the contribution due to flux boosting by measuring the flux densities of the injected sources used to calculate completeness f_{out} and take the ratio with their assigned fluxes f_{in} and check their variation as function of S/N. Flux boosting is negligible above 3σ for sources in high-rms fields. For sources in the lower-rms fields, it ranges from $f_{\text{out}}/f_{\text{in}}: 1.42$ to 1.05 for sources with an S/N from 0.5–6.5 σ .

Figure 4 shows the source counts obtained from the primarily serendipitous source sample (i.e., with $S/N > 3.75$) and from the high-confidence sample (i.e., with $S/N > 5.25$ in the lower-rms fields). The results are consistent with each other suggesting the details of the serendipitous sample selection do not significantly affect our conclusions. We compare our counts with those expected from models (Shimizu et al. 2012; da Cunha et al. 2013; Hayward et al. 2013), previously measured ALMA counts obtained for presumably unbiased populations (Hatsukade et al. 2013; Karim et al. 2013; Ono et al. 2014), and also with the results of Jones et al. (2015). These literature counts are converted to counts at $870 \mu\text{m}$ by using a modified blackbody (as in Hatsukade et al. 2013; Ono et al. 2014) assuming $\beta = 1.5$, $T_d = 35 \text{ K}$, and $z = 2.5$, which are typical values for SMGs (Coppin et al. 2008; Yun et al. 2012). Our counts are significantly in excess of both models and observations for field SMGs. However, within the uncertainties, they agree with the counts obtained by Jones et al. (2015), who find an excess of $6\times$ relative to blank fields on scales of $\lesssim 1 \text{ Mpc}$. Our counts imply an even stronger excess of $\sim 10\times$ relative to blank-sky surveys and are on much smaller

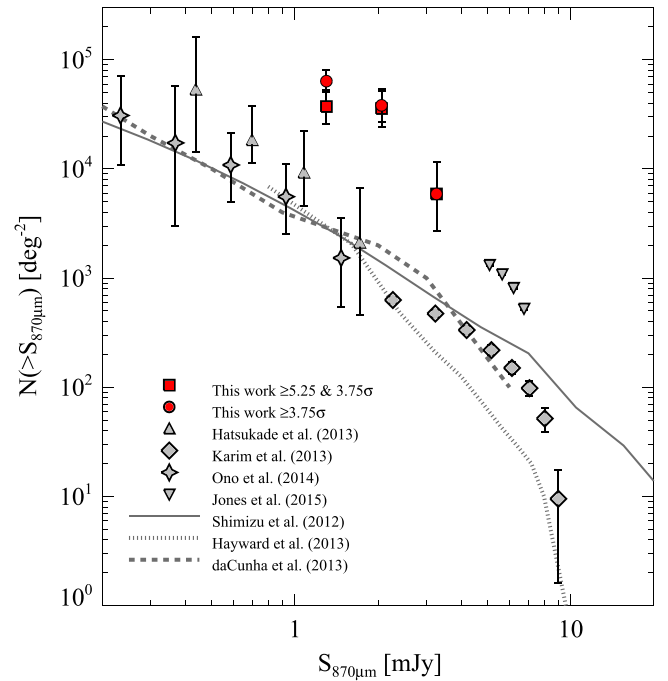


Figure 4. Integral source counts of SMGs around extremely red *WISE*/*NVSS* sources (red circles) obtained with ALMA observations at $870 \mu\text{m}$ with an $S/N > 3.75$. We also plot the counts obtained using the high-confidence limit (squares). We overplot the ALMA counts determined by Hatsukade et al. (2013) at 1.3 mm, Karim et al. (2013) at $870 \mu\text{m}$, and Ono et al. (2014) at 1.2 mm and the models of Shimizu et al. (2012), da Cunha et al. (2013), and Hayward et al. (2013). In addition, we include the counts obtained by Jones et al. (2015) toward a sub-sample of the same parent population of our targets. All of these results were scaled to $870 \mu\text{m}$ using a modified blackbody. For the Karim et al. (2013) counts, we applied a correction factor of $2\times$ underdensity of SMGs in the LESS field (Swinbank et al. 2014). Our counts are ~ 25 to $10\times$ stronger than the comparison models and observations toward blank fields and in agreement with the counts of Jones et al. (2015).

spatial scales compared to Jones et al. (2015; $< 150 \text{ kpc}$). Compared to the closest model (that of da Cunha et al. 2013), this excess is at the $\sim 5\sigma$ level.

5. DISCUSSION

What does an overdensity of $\gtrsim 10\times$ imply for our *WISE*/*NVSS*-selected $z \sim 1.7$ quasars? This is even stronger than the overdensity of $6\times$ around a comparable sample found in Jones et al. (2015) on scales of $\lesssim 1 \text{ Mpc}$. Since the counts of Jones et al. (2015) could be affected by unresolved sources (Karim et al. 2013), without flux density overlap, we cannot assess whether or not the small difference in level of overdensity as measured in this paper and in Jones et al. (2015) is significant. The drop in overdensity from scales of $< 150 \text{ kpc}$ to nearly 1 Mpc as sampled between the two papers is far weaker than expected based on local structures. For example, Budzynski et al. (2012) show that the surface density of galaxies in local groups and clusters drops by $\sim 100\times$ from roughly 100 kpc to 1 Mpc. This implied that the lack of significant clustering is also consistent with the angular distribution of sources as seen in both our paper and in Jones et al. (2015).

We looked for trends in the presence of serendipitous sources in a field vs. redshift, total luminosity, $870 \mu\text{m}$ flux (or just sub-millimeter detection of the central *WISE*/*NVSS* source), and radio power. We found no significant trends with respect to any of these properties of the central dusty quasar.

However, as discussed in Section 2, the ALMA sub-sample is lacking the most radio-loud sources in the parent *WISE*/*NVSS* sample, and therefore the range in radio power probed may be too small to detect any trends with the strength of the radio AGN.

Our galaxies are rare, hyper-luminous, obscured quasars, with significant dust masses⁹ (see L15) and by extension cold gas masses. This is similar to findings of HzRGs, including the Spiderweb (Iverson et al. 2012; Emonts et al. 2013). The large dust masses imply young objects that will likely evolve into red and dead ellipticals. This study, as well as Jones et al. (2015), suggests these sources reside in significantly overdense regions, but not yet fully formed clusters. The observed overdensity is in SMGs, which implies significant star formation, again similar to the much more radio-powerful Spiderweb galaxy (Dannerbauer et al. 2014). We show tentative signs of a dearth of gas-rich star-forming galaxies at the very centers of these potential protoclusters—potentially an early indication of morphological segregation in clusters. Upcoming *Spitzer*/*IRAC* imaging of these regions will help further explore this issue, as the mass-selected *IRAC* sources should show a more centrally concentrated angular distribution.

This study demonstrates the utility of environmental studies using archival ALMA images, which allow us to sample at high resolution the dense cores of potential protoclusters. Follow-up redshift studies are needed to confirm if we have indeed detected protoclusters, especially in the case of J151003.71–220311, which shows the highest overdensity of SMG sources.

6. CONCLUSIONS

We examined the near fields of 49 *WISE*/*NVSS*-selected dusty, hyper-luminous quasars at $\langle z \rangle > 1.7$, using ALMA 870 μm images. We found 23 additional SMG sources in 17 of these 49 fields. These imply a source density $\sim 10\times$ higher than expectations for field SMGs, consistent with previous studies in the fields of $z \sim 2$ QSOs and radio galaxies (Kodama et al. 2007; Venemans et al. 2007; Priddey et al. 2008; Stevens et al. 2010; Matsuda et al. 2011; Husband et al. 2013; Dannerbauer et al. 2014). Our results are consistent with Jones et al. (2015), although we focus on smaller spatial scales, sampling the dense inner cores of potential protoclusters.

We are grateful to B. Hatsukade and Y. Matsuda for useful discussions and A. Blain for a critical reading of an earlier draft of this manuscript. We also thank Y. Ono, I. Shimizu, and E. da Cunha for providing their counts and models. We thank the anonymous referee for useful feedback that helped improve this paper. A.S. is partially supported by NSF AST-1313206. This paper makes use of the following ALMA data: ADS/JAO.ALMA#2011.0.00397.S. ALMA is a partnership of ESO (representing its member states), NSF (USA) and NINS (Japan), together with NRC (Canada) and NSC and ASIAA

(Taiwan), in cooperation with the Republic of Chile. The joint ALMA Observatory is operated by ESO, AUI/NRAO and NAOJ. The National Radio Astronomy Observatory is a facility of the National Science Foundation operated under cooperative agreement by Associated Universities, Inc. Cosmology calculations in this paper were performed using the Ned Wright Cosmology Calculator.

REFERENCES

- Bertin, E., & Arnouts, S. 1996, *A&AS*, **117**, 393
 Blain, A. W., Smail, I., Iverson, R. J., Kneib, J.-P., & Frayer, D. T. 2002, *PhR*, **369**, 111
 Budzynski, J. M., Kaposov, S. E., McCarthy, I. G., McGee, S. L., & Belokurov, V. 2012, *MNRAS*, **423**, 104
 Coppin, K., Halpern, M., Scott, D., et al. 2008, *MNRAS*, **384**, 1597
 da Cunha, E., Walter, F., Decarli, R., et al. 2013, *ApJ*, **765**, 9
 Dannerbauer, H., Kurk, J. D., De Breuck, C., et al. 2014, *A&A*, **570**, AA55
 Emonts, B. H. C., Feain, I., Röttgering, H. J. A., et al. 2013, *MNRAS*, **430**, 3465
 Falder, J. T., Stevens, J. A., Jarvis, M. J., et al. 2011, *ApJ*, **735**, 123
 Fanidakis, N., Macciò, A. V., Baugh, C. M., Lacey, C. G., & Frenk, C. S. 2013, *MNRAS*, **436**, 315
 Geach, J. E., Murphy, D. N. A., & Bower, R. G. 2011, *MNRAS*, **413**, 3059
 Gladders, M. D., & Yee, H. K. C. 2005, *ApJS*, **157**, 1
 Glenn, J., Conley, A., Béthermin, F., et al. 2010, *MNRAS*, **409**, 109
 Hatsukade, B., Ohta, K., Seko, A., Yabe, K., & Akiyama, M. 2013, *ApJL*, **769**, L27
 Hayward, C. C., Narayanan, D., Kereš, D., et al. 2013, *MNRAS*, **428**, 2529
 Husband, K., Bremer, M. N., Stanway, E. R., et al. 2013, *MNRAS*, **432**, 2869
 Iverson, R. J., Dunlop, J. S., Smail, I., et al. 2000, *ApJ*, **542**, 27
 Iverson, R. J., Smail, I., Amblard, A., et al. 2012, *MNRAS*, **425**, 1320
 Iverson, R. J., Swinbank, A. M., Smail, I., et al. 2013, *ApJ*, **772**, 137
 Jarrett, T. H., Cohen, M., Masci, F., et al. 2011, *ApJ*, **735**, 112
 Jones, S. F., Blain, A. W., Lonsdale, C., et al. 2015, *MNRAS*, **448**, 3325
 Karim, A., Swinbank, A. M., Hodge, J. A., et al. 2013, *MNRAS*, **432**, 2
 Kodama, T., Tanaka, I., Kajisawa, M., et al. 2007, *MNRAS*, **377**, 1717
 Lidman, C., Rosati, P., Tanaka, M., et al. 2008, *A&A*, **489**, 981
 Lonsdale, C. J., Lacy, M. D., Kimball, A. E., et al. 2015, *ApJ*, submitted
 Matsuda, Y., Smail, I., Geach, J. E., et al. 2011, *MNRAS*, **416**, 2041
 McMullin, J. P., Waters, B., Schiebel, D., Young, W., & Golap, K. 2007, *adass XVI*, **376**, 127
 Mei, S., Holden, B. P., Blakeslee, J. P., et al. 2009, *ApJ*, **690**, 42
 Miley, G. K., Overzier, R. A., Zirm, A. W., et al. 2006, *ApJL*, **650**, L29
 Ono, Y., Ouchi, M., Kurono, Y., & Momose, R. 2014, *ApJ*, **795**, 5
 Peng, Y.-J., Lilly, S. J., Renzini, A., & Carollo, M. 2012, *ApJ*, **757**, 4
 Planck Collaboration Ade, P. A. R., Aghanim, N., et al. 2014, *A&A*, **571**, AA16
 Patanchon, G., Ade, P. A. R., Bock, J. J., et al. 2009, *ApJ*, **707**, 1750
 Priddey, R. S., Iverson, R. J., & Isaak, K. G. 2008, *MNRAS*, **383**, 289
 Poggianti, B. M., De Lucia, G., Varela, J., et al. 2010, *MNRAS*, **405**, 995
 Shimizu, I., Yoshida, N., & Okamoto, T. 2012, *MNRAS*, **427**, 2866
 Smail, I., Chapman, S. C., Blain, A. W., & Iverson, R. J. 2004, *ApJ*, **616**, 71
 Stevens, J. A., Iverson, R. J., Dunlop, J. S., et al. 2003, *Natur*, **425**, 264
 Stevens, J. A., Jarvis, M. J., Coppin, K. E. K., et al. 2010, *MNRAS*, **405**, 2623
 Swinbank, A. M., Simpson, J. M., Smail, I., et al. 2014, *MNRAS*, **438**, 1267
 Venemans, B. P., Röttgering, H. J. A., Miley, G. K., et al. 2007, *A&A*, **461**, 823
 Wylezalek, D., Galametz, A., Stern, D., et al. 2013, *ApJ*, **769**, 79
 Yan, L., Donoso, E., Tsai, C.-W., et al. 2013, *AJ*, **145**, 55
 Yuan, T., Nanayakkara, T., Kacprzak, G. G., et al. 2014, *ApJL*, **795**, LL20
 Yun, M. S., Scott, K. S., Guo, Y., et al. 2012, *MNRAS*, **420**, 957

⁹ Assuming all the 870 μm emission is thermal.